Research Article

Nano Research
2023, 16(1): 70–79

ISSN 1998-0124 CN 11-5974/O4
https://doi.org/10.1007/s12274-022-4950-x

Low-dimensional cobalt doped carbon composite towards wideband electromagnetic dissipation

Xiaodi Zhou[1,2], Biao Zhao[1] (✉), and Hualiang Lv[2] (✉)

[1] *School of Microelectronics, Fudan University, Shanghai 200433, China*
[2] *Willian G. Lowrie Department of Chemical and Biomolecular Engineering, The Ohio State University, Columbus, OH 43210, USA*

Received: 18 July 2022 / **Revised:** 17 August 2022 / **Accepted:** 23 August 2022

ABSTRACT

Composites composed of a carbon matrix decorated with a metal or metal oxide derived from zeolitic imidazolate frameworks (ZIFs) have been widely applied as suitable electromagnetic wave absorbers due to their high porosity and controllable morphology. However, achieving ideal absorption performance remains a challenge owing to the inadequate conductivity and high density of the metal components. Therefore, a temperature-controlling treatment was employed for the bimetal ZIFs, and the corresponding derivatives exhibited an excellent dissipation ability with a minimum reflection loss value of −54.3 dB and an effective bandwidth of 7.0 GHz at a thickness of 2.4 mm, which resulted from the strong dipole polarization behavior. Furthermore, after successfully controlling the Zn/Co ratio, the attenuation capability was greatly enhanced at a thickness of 1.4 mm, with bandwidths of 13.0–18.0 GHz. Overall, this work provides an ameliorated strategy for microwave absorption performance of carbon-based materials.

KEYWORDS

microwave absorption, bi-meta based absorber, single-atom, metal organic frameworks (MOFs) derived composite, dielectric relaxation

1 Introduction

With the rapid development and widespread popularization of wireless communication technology, the information era of 5th generation mobile networks (5G) has already arrived. However, while the electromagnetic (EM) waves that build bridges between wireless equipment greatly improve the speed of information transmission, the harm of redundant radiation to the surrounding environment and human health cannot be ignored [1–4]. Therefore, finding an efficient and economical strategy to address EM pollution is urgently needed. Currently, due to technological innovations in materials engineering, the design and synthesis of a desirable material for EM absorption have become of great interest. An ideal absorber should be lightweight and display great performance under a thin coating thickness.

In general, the attenuation mechanism of EM waves can be divided into magnetic and electric losses [5–7]. To maximize the magnetic loss capability, the main component of the absorber is commonly comprised of ferromagnetic metals (Fe, Co, and Ni) and their oxides [8, 9]. For example, Sui et al. fabricated hollow Fe_3O_4 particles with a minimum reflection loss (RL_{min}) of −55.1 dB and an effective bandwidth (f_E) of 4.7 GHz at a thickness under 2 mm and with a filler ratio of 70 wt.% [10]. Shen et al. synthesized FeCoNi@HC composites that exhibited a RL_{min} value of −61.1 dB and a f_E value of 5.5 GHz with a filler loading of 70 wt.% [11]. Although metal or metal-based materials exhibit a good EM absorption ability, their relatively high density (reflected as a large filler ratio) limits their practical application. For the electric loss, which is mainly related to conductivity, considering the factors of economy and lightness in weight, carbon-based materials appear to be the ideal candidate for the absorber material [12, 13]. For instance, Wang et al. designed a CNTs@PANi hybrid absorber through a longitudinal unzipping treatment and corresponding RL_{min} value reached −45.7 dB with a f_E value of 5.6 GHz at a thickness of 2 mm [14]. Flower-like graphene was fabricated by spray drying, prereduction, and annealing procedures, revealing a RL_{min} of −42.9 dB and a f_E of 5.6 GHz at a thickness under 2 mm [15]. However, the complex preparation processes and extreme synthesis conditions of such carbon-based materials hinder further exploration.

Recently, a carbon-based material derived from metal organic frameworks (MOFs), which were prepared by the self-assembly of metal ions and organic ligands, has attracted great attention. Due to their large porosity, low density, and uniform structure, MOFs have been widely applied in the fields of catalysis, sensing, energy storage, etc. [16–18]. In addition, among dozens of species of precursors, zeolitic imidazolate frameworks (ZIFs), particularly ZIF-8 and ZIF-67, stand out due to their simple preparation process, inexpensive raw materials, and strong stability [19, 20]. Interestingly, after a suitable pyrolysis treatment, the organic frameworks will decompose into a carbon matrix decorated with metal or metal oxides without structural collapse, and the derivatives often exhibit better conductivity and higher porosity, showing great potential for application in microwave absorption. Recently, Li and his group decorated carbon nanotubes (CNTs) with ZnO nanoparticles derived from ZIF-8. The product showed an enhanced electric loss ability [21] with a RL_{min} of −48.2 dB and

Address correspondence to Biao Zhao, zhao_biao@fudan.edu.cn; Hualiang Lv, yexuexun5309@163.com

a f_E of 6.0 GHz at a thickness of 3.0 mm. Similarly, Chen et al. hybridized CNTs with Co/CoO derived from ZIF-67; the RL_{min} value reached −53.1 dB with a broad f_E value of 4.0 GHz at a thickness of 2.5 mm [22]. Inspired by the analogous crystal structure of ZIF-8 and ZIF-67, Feng and his coworkers obtained a core–shell heterostructure of ZnO@NC/Co_3ZnC after annealing the bimetal ZIFs (BIZIFs) [23]. The composites exhibited a RL_{min} of −62.9 dB and a f_E of 5.5 GHz at a thickness of 2.2 mm. Although the above work showed large effective bandwidths, the EM absorption performance should be further improved while maintaining a reduced thickness.

Herein, we employed a temperature-controlled pyrolysis procedure to the BIZIFs and obtained a series of N-doped carbon-based composites. The high-temperature carbonization would enhance the degree of graphitization of the as-prepared carbon matrix, thus improving the conductivity and subsequent electrical loss ability. Additionally, the high-temperature evaporation of the Zn component would greatly increase the porosity of the composites, thereby meeting the requirement of lightweight for the ideal absorber. Furthermore, the Co element would exhibit a uniform distribution in the framework during the evaporation process. Subsequently, regulation of the ratio of Zn to Co elements was further implemented to ameliorate the EM absorbing performance at a reduced thickness.

2 Experimental

2.1 Materials

Zinc nitrate hexahydrate ($Zn(NO_3)_2{\cdot}6H_2O$, 99%), cobalt nitrate hexahydrate ($Co(NO_3)_2{\cdot}6H_2O$, 99%), 2-methylimidazole (MeIM, 99%), methanol (99.9%), and ethanol (99%) were purchased from the Aladdin company. All chemical reagents were analytically pure and used without further purification.

2.2 Preparation of the BIZIF-4 precursor

Firstly, 640 mg of $Zn(NO_3)_2{\cdot}6H_2O$ and 170 mg of $Co(NO_3)_2{\cdot}6H_2O$ (keeping the ratio of Zn and Co elements equals 4) were dissolved in 30 mL of methanol. Then 526 mg of MeIM was added to the solution. After fully dissolved under the ultrasonic dispersion, the mixed solution was rested at the room temperature for 16 h. Finally, the pale pink powders were obtained by centrifugated at 3,500 rpm, washed with ethanol for several times, and dried at 80 °C for 10 h. The collected sample was denoted as BIZIF-4.

2.3 Preparation of CN-4 composites

200 mg of prepared BIZIF-4 precursors was put in the ceramics boat and annealed at different temperature (700, 800, 900, 1,000, and 1,100 °C) for 2 h under the N_2 atmosphere. After cooled naturally, the corresponding samples were denoted as CN-4-700, CN-4-800, CN-4-900, CN-4-1000, and CN-4-1100, respectively.

2.4 Preparation of ZIF-8, ZIF-67, BIZIF-2, and corresponding derivatives

The syntheses of ZIF-8, ZIF-67, and BIZIF-2 precursors were similar with the BIZIF-4 sample, except for modifying the dosage of zinc and cobalt salts (814 and 0; 545 and 256; and 0 and 796 mg). After collecting as-synthesized powders, a carbonization treatment, similar to the preparation process of CN-4-1000, was applied to each precursor. The corresponding products were denoted as CN-Zn-1000, CN-Co-1000, and CN-2-1000, respectively.

2.5 Characterization

The morphology and structure of composites were investigated by a field-emission scanning electron microscopy (FESEM, JSM-7600F) and a high-angle annular dark-field scanning transmission electron microscopy (HADDF-STEM) with its corresponding energy-dispersive spectroscopy (EDS) mapping analyses (Tecnai G2 20U-TWIN). The characterization of Fourier transform infrared (FTIR) and Raman spectra were recorded by BRKR VERTEX 80V Fourier transform infrared spectroscopy and Themor DXR532 Raman spectrometer (wavenumber = 531 cm^{-1}), respectively. The crystallite information was analyzed by Rigaku Ultima IV diffractometer (X-ray diffraction (XRD)) using Cu-Kα radiation (40 kV, 40 mA, λ = 1.5418 Å). X-ray absorption fine structure (XAFS) measurements were collected at the Singapore synchrotron light source (SSLS) with a ring electron current of 250 mA at 3.5 GeV. The X-ray photoelectron spectrum (XPS) was performed on Escalab 250Xi spectrometer. The electromagnetic properties, the relative complex permittivity (ε_r) and permeability (μ_r) within the frequency range of 2–18 GHz, were investigated by a VNA N5224A vector network analyzer (Agilent) based on the coaxial reflection/transmission method according to the standard of ASTM 5568. The toroidal-shaped samples were prepared by mixing 30 wt.% of as-prepared composites with paraffin wax and pressed into cylindrical rings with inner and outer diameters of 3.04 and 7 mm, respectively.

3 Results and discussion

The synthesis strategy of CN composites derived from the BIZIF-4 precursor is illustrated in Fig. 1. The BIZIF-4 sample was obtained by the self-assembly reaction between organic ligands (MeIM) and metal ions (Zn^{2+} and Co^{2+}). Subsequently, the as-prepared precursor was treated by pyrolysis, transforming the organic coordinated frame into an N-doped carbon matrix decorated with metal or metal oxides. It should be noted that during carbonation at high temperatures, evaporation of the Zn phase, which was derived from the reduction of ZnO with the carbon matrix, was beneficial for the dispersion of Co and could promote the formation of Co single atoms.

As shown in Figs. 2(a) and 2(b), the as-synthesized BIZIF-4 precursors exhibited a uniform distribution and showed a rhombic dodecahedral shape with a diameter of about 300 nm, similar to previous reports [24, 25]. In Fig. 2(c), the positions of all diffraction peaks in the precursors were in good agreement with the simulated XRD pattern of ZIF-8 or ZIF-67, in which the identical XRD patterns of ZIF-8 and ZIF-67 resulted from their isostructural frameworks [26]. The FTIR analysis is shown in Fig. 2(d). For the pure organic ligand, MeIM, a broad peak in the range of 2,200–2,300 cm^{-1} can be observed, corresponding to the vibration of the hydrogen bond formed between two nearby ligands (N–H=N). The peak at around 1,800 cm^{-1} could be attributed to the stretching mode of such intermolecular hydrogen bonding [27]. Conversely, both abovementioned peaks were hardly observed in the spectra of the BIZIF-4 precursors. In addition, a new diffraction peak at 420 cm^{-1} could be ascribed to the stretching vibration of the coordination bond of metal ions and organic ligands (Zn–N and Co–N) [28]. Therefore, according to the above analysis, the successful fabrication of the BIZIF-4 precursor could be confirmed.

The morphology after pyrolysis at different temperatures was investigated, as shown in Figs. 3(a)–3(e). The individual polyhedron-like shape could still be detected for the CN-4-700, CN-4-800, CN-4-900, and CN-4-1000 composites. For CN-4-1100, however, a slight contraction phenomenon was exhibited, which might result from the continuous generation and subsequent release of gaseous oxides and nitrides at a high degree of carbonization [29]. Furthermore, the images of CN-4-700 and

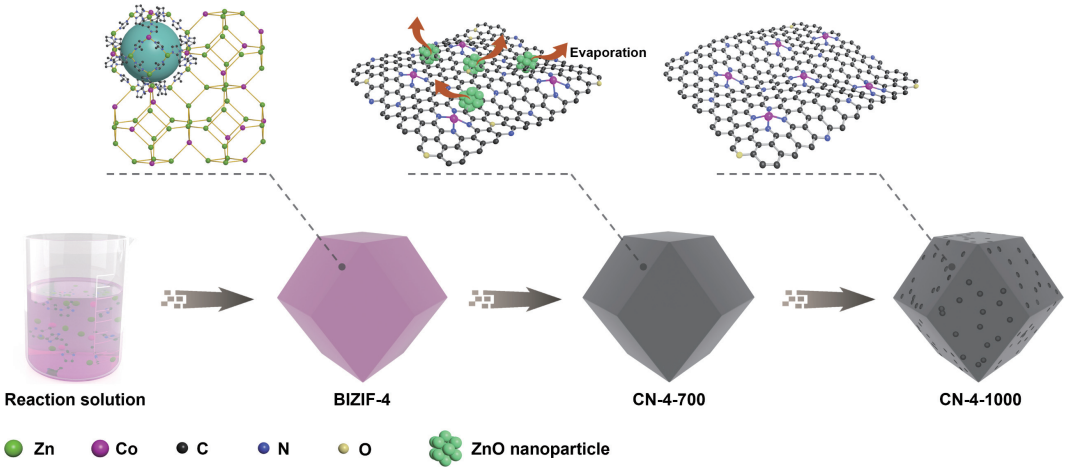

Figure 1 Schematic illustration of the synthesis process for CN-4-1000.

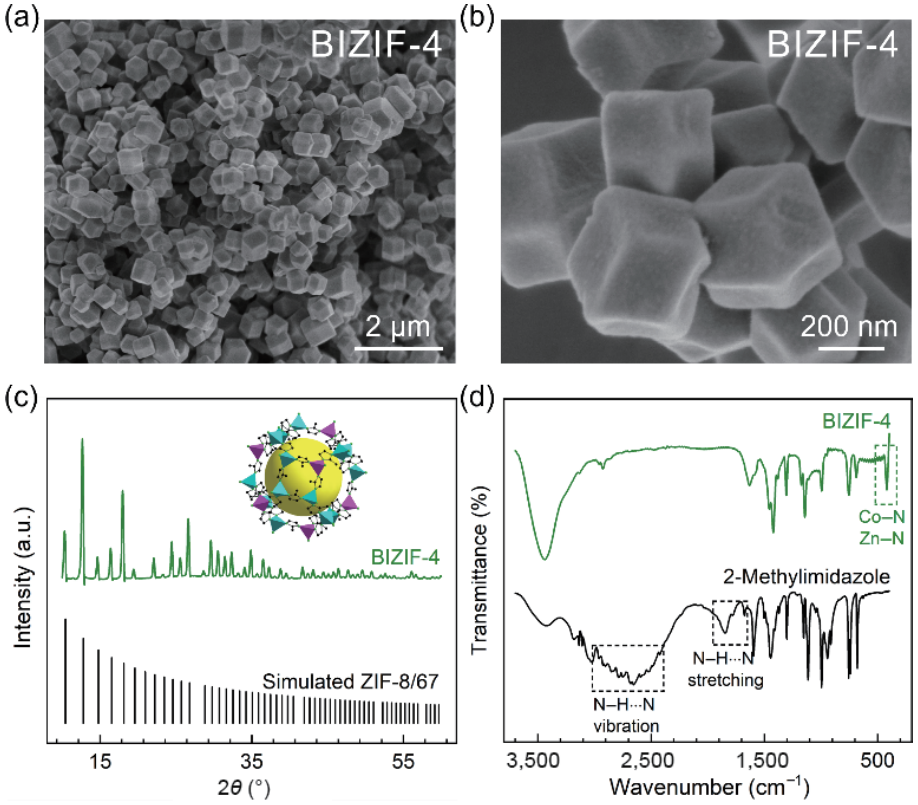

Figure 2 Surface and composite characterization of BIZIF-4 precursor: (a) and (b) FESEM images of BIZIF-4; (c) XRD patterns of BIZIF-4 and simulated ZIF-8/67; and (d) FTIR spectra of BIZIF-4 and pure 2-methylimidazole.

CN-4-800 presented a relatively low resolution compared with those of CN-4-900 and CN-4-1000. This could be attributed to the presence of ZnO with low conductivity at the moderate annealing temperatures, which would be further demonstrated below. The solid polyhedral structure was affirmed in Fig. 3(f). Interestingly, for CN-4-1000 (Fig. 3(g)), no obvious lattice fringe could be observed in the HAADF-STEM image; however, some bright points (marked with red dotted circles) dispersed on the carbon matrix were observed. This phenomenon could be explained by the formation of small nanoparticles or even single atoms. Therefore, extended X-ray absorption fine structure (EXAFS) spectroscopy was applied. As shown in Fig. 3(h), in the *R*-space of the EXAFS spectra, the prominent peak was located at around 1.4 Å, demonstrating the coordination mode of Co atoms surrounded by nitrogen atoms in N-doped carbon, further demonstrating that the above points were Co single atoms [30, 31]. Figure 3(i) revealed the homogeneous distribution of Co, C, N, and O elements in CN-4-1000.

The XRD patterns of the CN-4 derivatives are revealed in Fig. 4(a). For CN-4-700, the characteristic peaks at 31.8°, 34.4°, 36.3°, 47.5°, 56.6°, 62.9°, 66.4°, 68.0°, and 69.1° could be indexed to the ZnO phase (JCPDS No. 36-1415). However, in the CN-4-800 pattern, the characteristic peaks of ZnO became weak and a broad peak of amorphous carbon at about 25° was detected resulting from the partial evaporation of the ZnO phase [32, 33]. After further increasing the carbonization temperature (for CN-4-900, CN-4-1000, and CN-4-1100), the peaks of ZnO could not be observed and the diffraction peak of carbon shifted to 26°, indicating the formation of graphitized carbon. Interestingly, none of the peaks related to Co or Co oxides has been identified in any of the composites. This abnormal phenomenon again confirmed the formation of Co single atoms, whose sizes were below the detection limit of the XRD instrument [34, 35].

As illustrated in Fig. 4(b), for the BIZIF-4 precursor, characteristic peaks (marked with asterisks) at around 1,430, 1,300, 1,140, 996, and 760 cm^{-1} were generated by the in-plane and out-

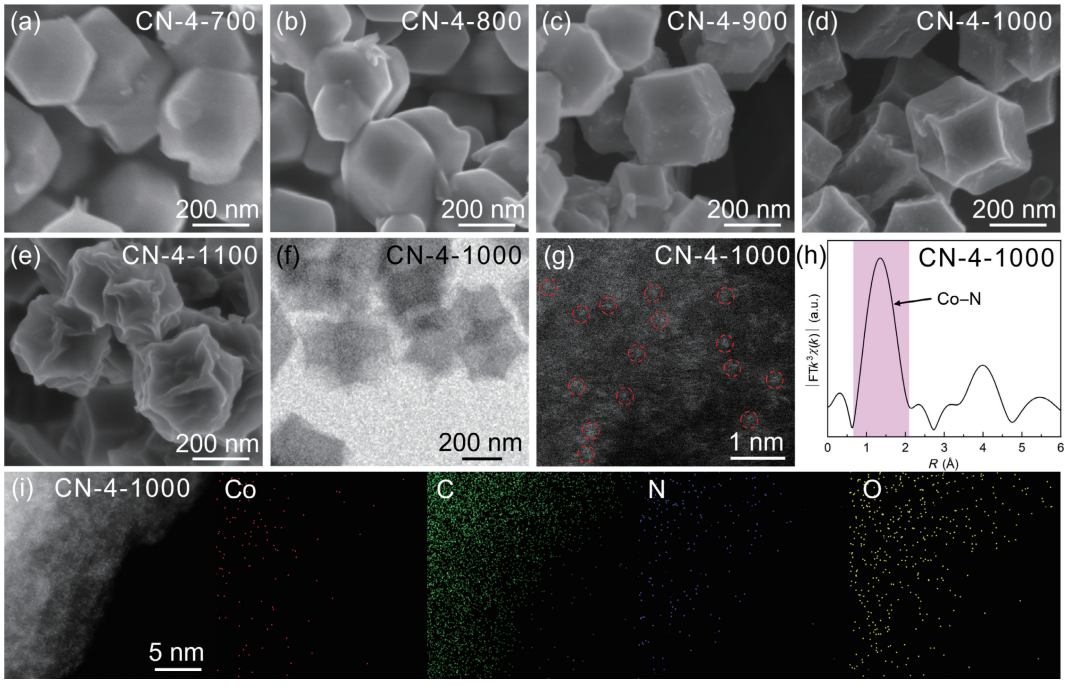

Figure 3 Surface and interior morphology analysis of CN-4 composites: FESEM images of CN-4-700 (a), CN-4-800 (b), CN-4-900 (c), CN-4-1000 (d), CN-4-1100 (e); (f) TEM image of CN-4-1000; (g) HADDF-STEM image of CN-4-1000 composite, the Co single atoms are marked with red dotted circles; (h) k^3-weighted $\chi(k)$ function of the EXAFS spectrum of CN-4-1000; and (i) the element mapping images of Co, C, N, and O elements.

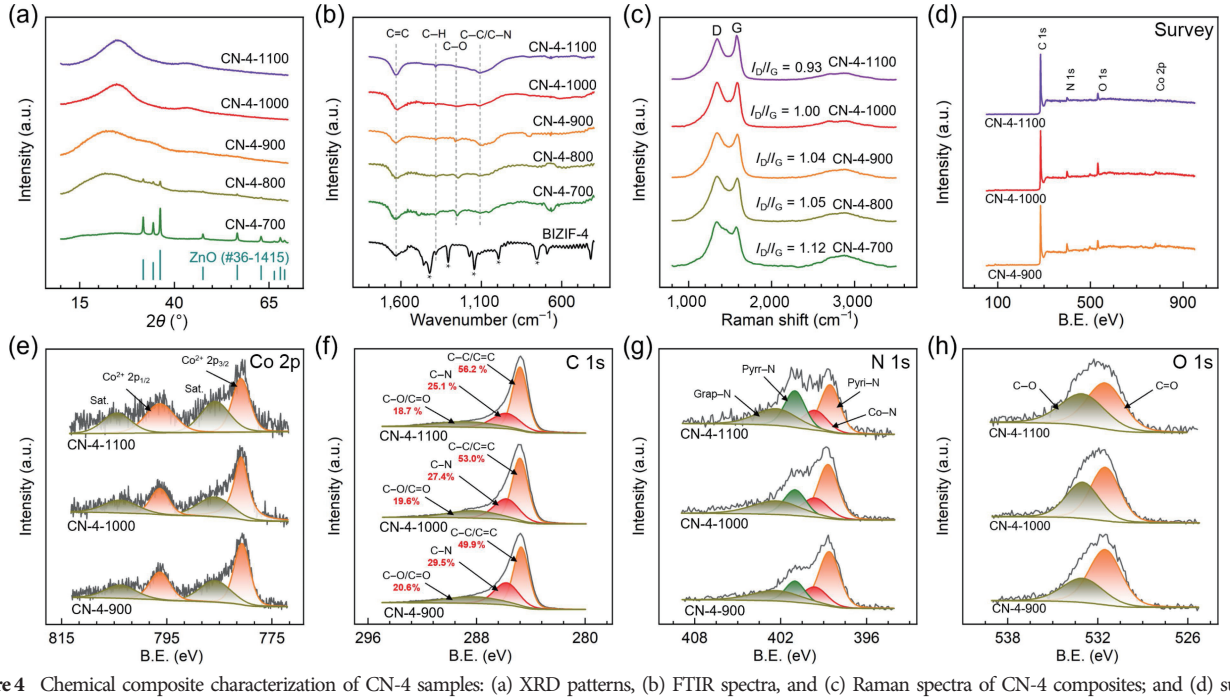

Figure 4 Chemical composite characterization of CN-4 samples: (a) XRD patterns, (b) FTIR spectra, and (c) Raman spectra of CN-4 composites; and (d) survey spectra and high resolution XPS spectra of (e) Co 2p, (f) C 1s, (g) N 1s, and (h) O 1s of CN-4-900, CN-4-1000, and CN-4-1100 composites, respectively.

of-plane vibration of the organic ligand [36]. After the annealing treatment, all these peaks disappeared and the stretching modes of C=C, C–H, C–O, and C–C/C–N at 1,620, 1,380, 1,250, and 1,105 cm^{-1}, respectively, could be detected in all of the derivatives, indicating the transformation from an organic framework to the main carbon phase [37]. Furthermore, the graphitization degree of the carbon matrix was investigated by Raman spectroscopy. In general, a high degree of graphitized carbon indicates a high electric conductivity, which would greatly influence the electromagnetic properties and final dissipation performance. In Fig. 4(c), two prominent peaks, the D-band (1,350 cm^{-1}) and G-band (1,580 cm^{-1}), could be observed for all derivatives, which again confirmed the existence of the carbon matrix. Typically, the degree of graphitization in carbon can be evaluated by the intensity ratio of the D-band to the G-band (I_D/I_G) [38, 39]. With the rising annealing temperature, the I_D/I_G values gradually decreased from 1.12 to 0.99, revealing an increase in the degree of graphitization.

The surface bonds of the as-prepared derivatives were analyzed by XPS measurement. The survey spectra of CN-4-900, CN-4-1000, and CN-4-1100 are shown in Fig. 4(d), exhibiting the presence of C, N, O, and Co elements. In detail, in Fig. 4(e), the peaks located at 780.8 and 796.3 eV could be ascribed to Co(II), caused by the coordination mode of Co–N and the partial oxidation of Co [40]. In addition, the fluctuating curves of the Co 2p spectra indicated the low content of the Co element. The

characteristic signals at 284.8, 285.8, and 288.2 eV (Fig. 4(f)) were related to C–C/C=C, C–N, and C–O/C=O bonds, respectively [41]. Specifically, the increasing content of C–C/C=C (49.9%–56.2%) and the decreasing proportions of C–N (29.5%–25.1%) and C–O/C=O (20.6%–18.7%) could be attributed to further graphitization as the temperature increased, which was consistent with the Raman spectra analysis. The main peaks at 398.7, 399.6, 401.0, and 402.3 eV (Fig. 4(g)) corresponded to pyridinic–N, Co–N, pyrrolic–N, and graphitic–N bonds, respectively [42]. The XPS spectra of the O element are shown in Fig. 4(h), confirming the existence of C=O (531.5 eV) and C–O (533.0 eV) bonds within the composites [43].

The EM dissipation performance of as-synthesized NC-4 derivatives was studied by the reflection loss (RL) value. Generally, the frequency-dependent RL value, according to the coaxial theory, could be calculated by following equations [44–46]

$$Z_{in} = Z_0\sqrt{\mu_r/\varepsilon_r}\tanh[j(2\pi fd/c)\sqrt{\mu_r\varepsilon_r}] \quad (1)$$

$$RL\,(dB) = 20\log[(Z_{in} - Z_0)/(Z_{in} + Z_0)] \quad (2)$$

where Z_{in} and Z_0 are the impedance values of the tested absorber and free space, ε_r and μ_r are the electromagnetic parameters of complex permittivity and permeability, respectively, j is the imaginary unit, f is the corresponding frequency of EM waves, d is the thickness of the absorber, and c is the velocity of EM waves in free space. Considered the economic and practical factors, for an ideal absorber, the related effective absorption region (f_E), representing the width of frequency band where RL value < −10 dB, should be designed to cover a broad region, and the thickness of absorption layer should be reduced to within 2 mm. The EM performance of samples was investigated in Fig. 5. In Figs. 5(a)–5(e), within the thickness of 1–5 mm, the minimum RL values (RL_{min}) of CN-4-700, CN-4-800, CN-4-900, CN-4-1000, and CN-4-1100 were −3.8, −4.4, −52.3, −54.3, and −5.4, respectively. Altogether, CN-4-700, CN-4-800, and CN-4-1100 exhibited the poor dissipation performance. Although CN-4-900 displayed a low RL_{min} value (−52.3 dB), its corresponding thickness was too thick. Therefore, the further analysis of CN-4-1000 is shown in Fig. 5(f). It could be found that the maximum f_E value of CN-4-1000 was 7.0 GHz (11.0–18.0 GHz) with a corresponding thickness of 2.4 mm.

The in-depth insight of the EM parameters and dissipation mechanisms are illustrated in Fig. 6. In general, ε' represents the storage ability of electric energy, while ε'' represents the dielectric-loss capability of microwaves. Notably, ε' could be considered as positively correlated to the electrical conductivity or the degree of graphitization of the composites [47, 48]. In Fig. 6(a), the ε' values of CN-4-700 and CN-4-800 were in the ranges of 2.9–2.6 and 3.7–3.2, respectively. The low values could be ascribed to the presence of the low-conductivity phase (ZnO) and the high content of amorphous carbon. After the high-temperature treatment, an obvious increase could be detected for CN-4-900 (6.0–4.5) and CN-4-1000 (9.5–4.6), which might be due to the volatilization of ZnO and graphitization of the carbon matrix. When annealed at 1,100 °C, the ε' value significantly increased to 58.8–12.7.

The ε'' parameters of the CN-4 composites (shown in Fig. 6(b)) displayed a similar trend to the ε' parameters and were in the ranges of 0.3–0.0, 0.6–0.1, 2.2–0.5, 4.5–2.1, and 57.6–17.8. In addition, Fig. 6(c) shows the increment of the tangent loss value ($\varepsilon''/\varepsilon'$), indicating the enhancement of the dielectric-loss capability with the increase in temperature. Overall, the poor EM performance of CN-4-700 and CN-4-800 might be caused by the low value of the dielectric properties. For CN-4-900 and CN-4-1000, the dissipation of EM waves was improved because of the increase in ε' and ε''. However, for CN-4-1100, when the permittivity value was excessively enhanced, no absorption performance could be observed due to the impedance mismatching [49, 50].

Next, the microwave dispersive behavior was explored by analyzing the relationship between ε' and ε''. In the typical Debye-theory, in the curve of ε' versus ε'', an approximate semicircle, usually denoted as Cole–Cole semicircle, represents one type of polarization relaxation process within absorbers [51–53]. The theory is derived from the formula of complex permittivity [54–56]

$$\varepsilon_r = \varepsilon_\infty + \frac{\varepsilon_s - \varepsilon_\infty}{1 + j2\pi f\tau} = \varepsilon' - j\varepsilon'' \quad (3)$$

where ε_∞ and ε_s are relative dielectric permittivity and static permittivity, and τ represents the corresponding polarization relaxation time at high-frequency limit. With the separation of

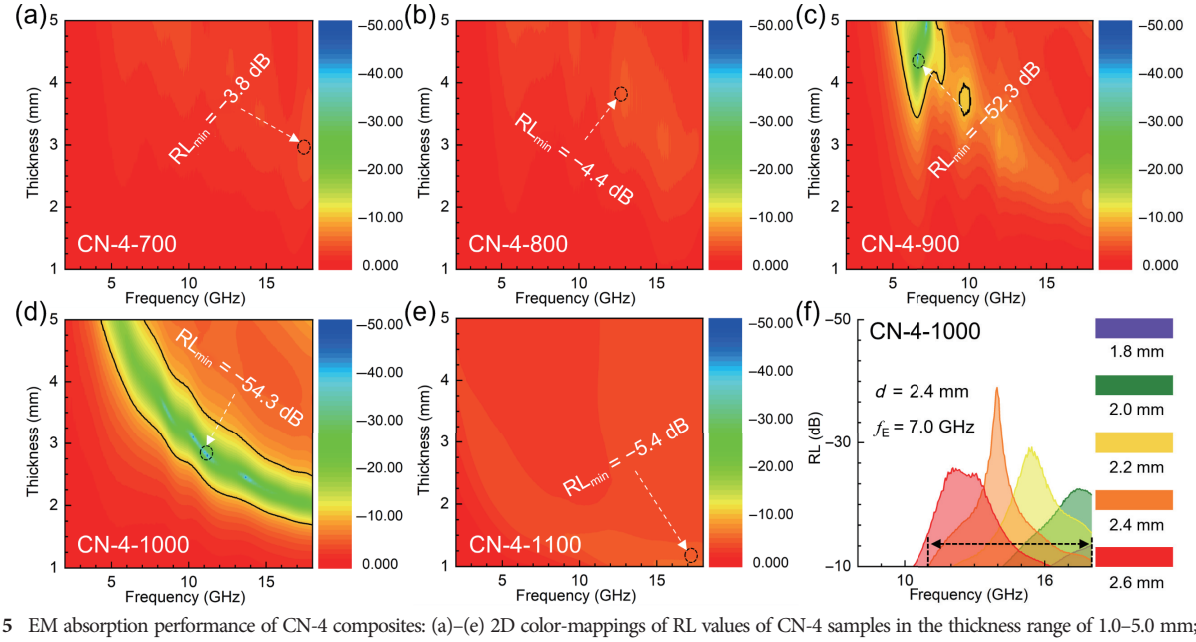

Figure 5 EM absorption performance of CN-4 composites: (a)–(e) 2D color-mappings of RL values of CN-4 samples in the thickness range of 1.0–5.0 mm; and (f) the plot of RL value < −10 dB of CN-4-1000 under the range of 1.8–2.6 mm.

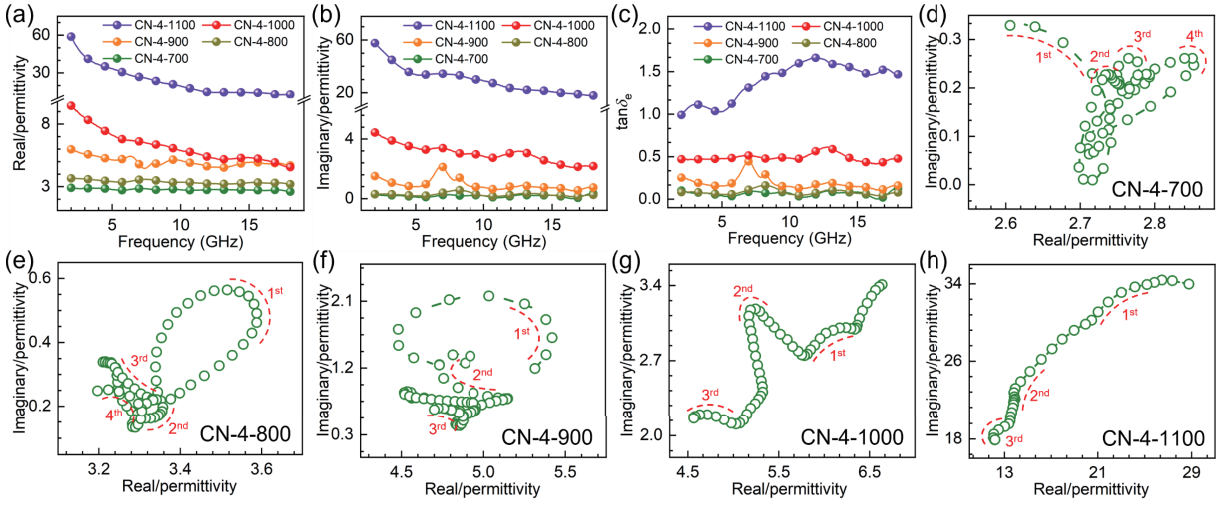

Figure 6 Investigation of dielectric parameters: (a) and (b) the real and imaginary part of permittivity and (c) dielectric loss tangent values of CN-4 composites; and (d)–(h) the Cole–Cole polarization circles of CN-4-700, CN-4-800, CN-4-900, CN-4-1000, and CN-4-1100 in the frequency range of 6.0–18.0 GHz.

variables, ε' and ε'' can be expressed by following equations [57–59]

$$\varepsilon' = \varepsilon_\infty + \frac{\varepsilon_s - \varepsilon_\infty}{1 + (2\pi f)^2 \tau^2} \quad (4)$$

$$\varepsilon'' = \varepsilon_\infty + \frac{2\pi f \tau (\varepsilon_s - \varepsilon_\infty)}{1 + (2\pi f)^2 \tau^2} \quad (5)$$

Combining Eqs. (4) and (5), the correlation of ε' and ε'' can be rewritten as following

$$(\varepsilon' - \varepsilon_\infty)^2 + (\varepsilon'')^2 = (\varepsilon_s - \varepsilon_\infty)^2 \quad (6)$$

Therefore, the Debye relaxation process could be studied by identifying Cole–Cole semicircles. As illustrated in Figs. 6(d)–6(h), the ε'–ε'' curves of CN-4 derivatives were displayed in the frequency range of 6.0–18.0 GHz. In detail, for CN-4-700 and CN-4-800, four Cole–Cole semicircles could be observed, which could be attributed to the polarization behavior of Zn–O bond in the ZnO phase and C–O, C–N, Co–N bonds in carbon matrix. After increasing carbonization temperature and fully vaporization of ZnO composite, three types of relaxation processes, C–O, C–N, and Co–N, were still detected for CN-4-900, CN-4-1000, and CN-4-1100. Therefore, the EM absorption performance of CN-4 composites could be mainly contributed to the polarization-dissipation behaviors of polar covalent bonds.

Although CN-4-1000 showed a broad effective absorption band, its corresponding thickness was outside of the ideal range (within 2 mm), which would limit its future practical utilization. Hence, a series of BIZIF derivatives were synthesized by controlling the Zn/Co ratio. In Fig. 7, all of the as-prepared precursors (ZIF-8, BIZIF-2, and ZIF-67) exhibited a well-dispersed rhombic dodecahedron shape, and the XRD patterns revealed similar characteristic peaks to BIZIF-4, suggesting the successful construction of the typical framework. The morphologies of the derivatives were investigated after annealing at 1,000 °C, as shown in Fig. 8. In detail, CN-Zn-1000, CN-4-1000, and CN-2-1000 maintained the original individual geometric skeleton (Figs. 8(a)–8(f)). However, for CN-Co-1000, the framework began to collapse and considerable crosslinking between particles could be detected, as shown in Figs. 8(g) and 8(h). To explore the reason, an in-depth discussion is presented below.

As shown in Fig. 9(a), the XRD pattern revealed only a broad peak of carbon at about 25° for CN-Zn-1000, CN-4-1000, and CN-2-1000, due to the vaporization of the ZnO composites and the formation of a Co single atom. In contrast, for CN-Co-1000, two

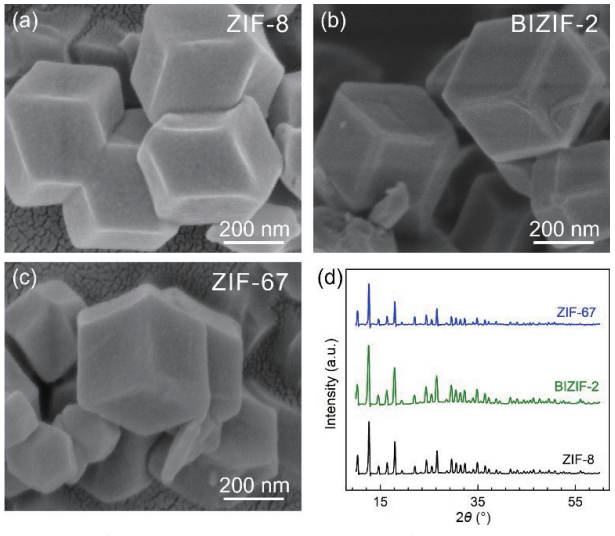

Figure 7 Surface and composite characterization of ZIF-8, BIZIF-2, and ZIF-67 precursors: FESEM images (a)–(c), and XRD patterns (d) of synthesized ZIF-8, BIZIF-2, and ZIF-67 precursors.

characteristic peaks at 44.2° and 51.5° were present, corresponding to the (110) and (200) planes, respectively, of the metallic Co phase (JCPDS No. 15-0806). In addition, the carbon-related peak shifted to 26° and became narrow and sharp, suggesting a high content of graphitized carbon. In addition, as illustrated in Fig. 9(b), the Raman spectra showed that with the increase in Co content, the I_D/I_G ratio decreased from 1.02 to 0.99. For CN-Co-1000, the ratio significantly plummeted to 0.56, and a sharp peak of 2D was detected, indicating the formation of graphene with few defects [60]. Above all, compared with CN-Zn-1000, CN-4-1000, and CN-2-1000, CN-Co-1000 exhibited an extremely high content of graphitized carbon, which could be attributed to the crystal effect of Co nanoparticles [61]. Therefore, such a conclusion could explain that the collapse of the framework and the crosslinking of nanoparticles resulted from the graphitization of CN-Co-1000.

Next, the chemical bonds were analyzed by XPS measurement. Figure 9(c) shows that CN-4-1000, CN-2-1000, and CN-Co-1000 were composed of C, N, O, and Co elements, while CN-Zn-1000 was comprised of C, N, and O elements. In the Co 2p spectra, as shown in Fig. 9(d), except for the Co(II) and corresponding satellite peaks, metallic Co peaks at 778.7 and 793.8 eV were also detected for CN-Co-1000. In addition, with the increase in Co content, the proportions of C–N (29.2%–19.2%) and C–O/C=O (19.7%–14.6%) decreased and the ratio of C–C/C=C bonds

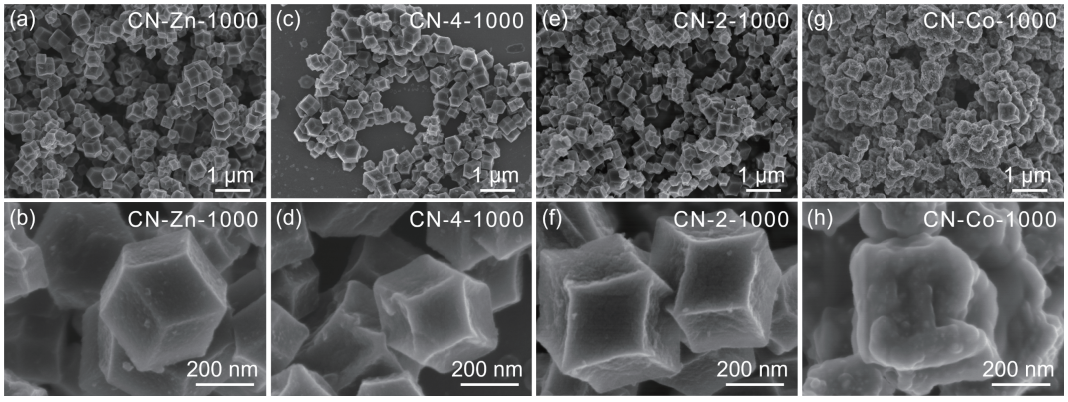

Figure 8 Surface structure characterization: FESEM images of CN-Zn-1000 (a) and (b); CN-4-1000 (c) and (d); CN-2-1000 (e) and (f); and CN-Co-1000 (g) and (h).

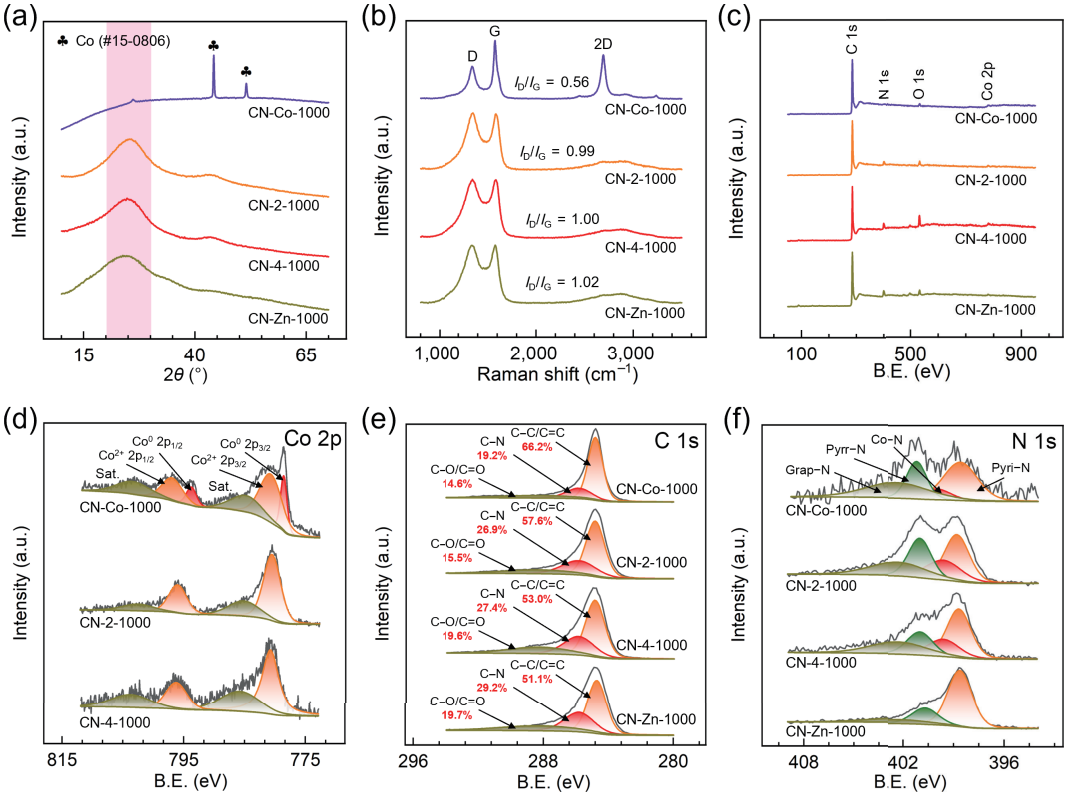

Figure 9 Characterization of chemical bonds and crystal structure: (a) XRD patterns; (b) Raman spectra; (c) survey spectra; and high resolution XPS spectra of (d) Co 2p, (e) C 1s, and (f) N 1s of CN-Zn-1000, CN-4-1000, CN-2-1000, and CN-Co-1000 samples.

(51.1%–66.2%) gradually increased (Fig. 9(e)). In Fig. 9(f), typical peaks of pyridinic–N, pyrrolic–N, and graphitic–N bonds were observed for all the composites. Notably, the Co–N bond was detected excluding CN-Zn-1000, indicating the complete evaporation of the Zn element and the absence of Zn single atoms. Overall, the conclusions derived from XPS spectra were in agreement with the XRD and Raman analyses.

After regulating the ratio of Zn to Co elements, the corresponding EM attenuation capability was explored (Fig. 10). As shown in Figs. 10(a) and 10(b), the ε' values for CN-Zn-1000, CN-4-1000, CN-2-1000, and CN-Co-1000 ranged from 3.7–3.1, 9.5–4.6, 22.2–9.7, and 12.9–8.1, respectively, while the ε'' values changed to 0.9–0.3, 4.4–2.1, 12.7–5.6, and 5.2–2.2, respectively. Interestingly, based on the previous analysis, CN-Co-1000 should have exhibited the highest permittivity value due to the high degree of graphitization. This abnormal phenomenon could be explained by the collapse and considerable crosslinking of nanoparticles during carbonization and thus resulted in the high density of CN-Co-1000, which greatly lowered the volume fraction of as-prepared composites in the paraffin matrix. The two-dimensional (2D) RL mapping revealed the EM performance (Figs. 10(c)–10(f)). No absorption capability was observed for CN-Zn-1000, and the effective absorption ranges of CN-2-1000 and CN-Co-1000 were shifted to reduced thicknesses as compared with CN-4-1000. Considering the requirements of an ideal absorber, the f_E values within the thickness of 2 mm were further investigated (Figs. 10(g)–10(i)). CN-4-1000 exhibited moderate performance with a maximum f_E value of 3.8 GHz at a thickness of 2.0 mm, while CN-2-1000 and CN-Co-1000 showed better EM dissipation ability with a f_E value of 5.0 GHz at a thickness of 1.4 mm and 3.2 GHz at a thickness of 1.8 mm, respectively. Therefore, after controlling the composition of Zn and Co elements in the synthesis of the precursor, the EM absorbing performance of the related derivative was enhanced to reach a larger f_E value at a reduced thickness.

4 Conclusions

In summary, a sequence of carbon matrix decorated with Co and/or Zn elements derived from BIZIF-4 precursor has been successfully fabricated through the temperature-controlling

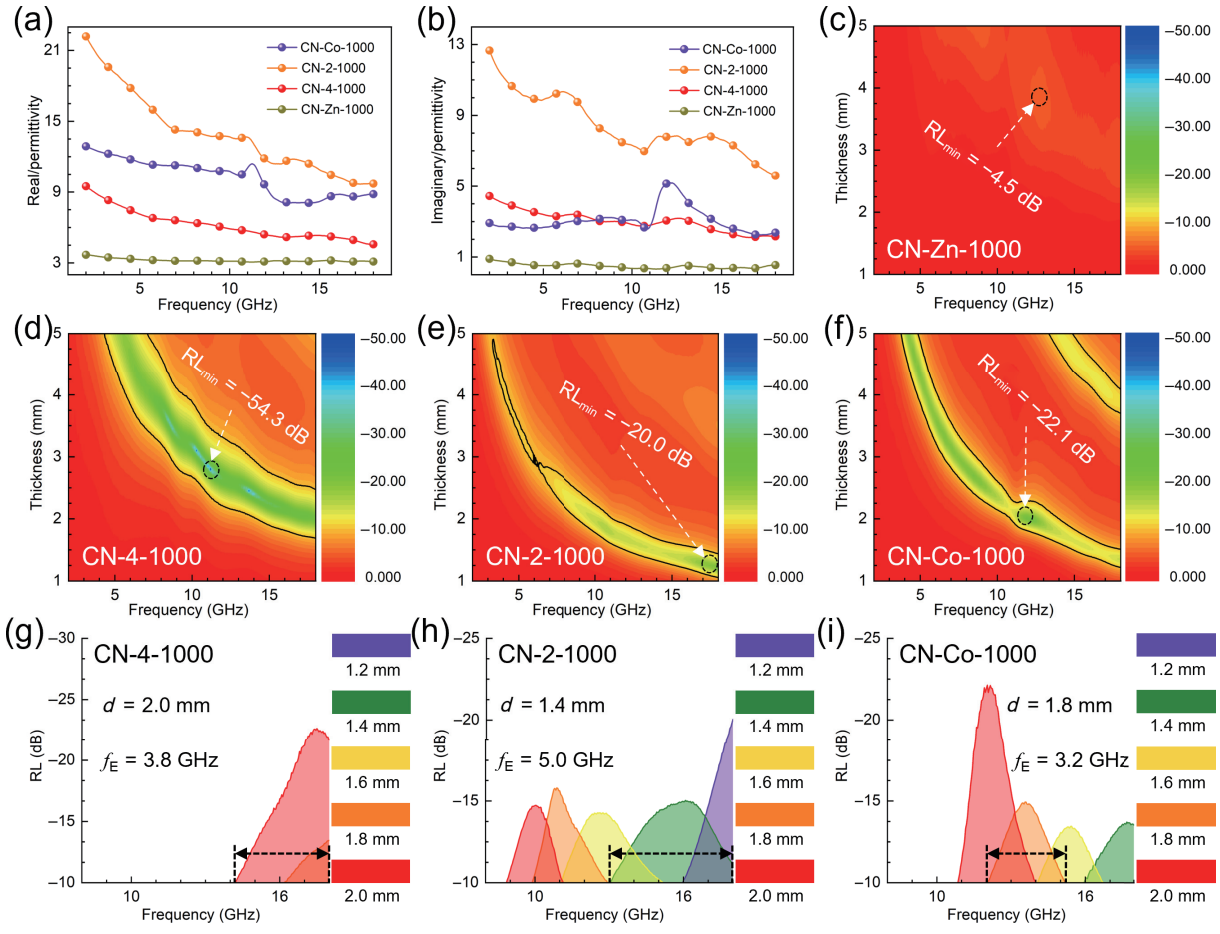

Figure 10 Investigation of EM dissipation performance: (a) and (b) the real and imaginary part of permittivity, (c)–(f) 2D color-mappings of reflection loss for CN-Zn-1000, CN-4-1000, CN-2-1000, and CN-Co-1000 samples; and (g)–(i) the curves of reflection values of CN-4-1000, CN-2-1000, and CN-Co-1000 within the thickness of 2 mm.

treatment. After fully evaporating of Zn component and with a suitable graphitized degree, the CN-4-1000 sample exhibited an advantageous absorption performance with a RL_{min} value of −54.3 dB and a broad effective bandwidth of 7.0 GHz under the thickness of 2.4 mm, which was attributed to the enhanced electric loss capability. Next, after regulating the ratio of Zn/Co elements, the attenuation performance was significantly improved under the thin thickness. Especially, the CN-2-1000 revealed an excellent EM dissipation ability that the f_E value reached 5.0 GHz at 1.4 mm. Overall, this work demonstrated that the temperature-controlled and component-regulated procedure could further enhance the EM absorption performance of existing absorbers.

Acknowledgements

The authors are thankful for the financial supports of the Science Foundation for The Excellent Youth Scholars of Henan Province (No. 212300410089), the Foundation for University Youth Key Teachers of Henan Province (No. 2020GGJS170), and the Support Program for Scientific and Technological Innovation Talents of Higher Education in Henan Province (No. 21HASTIT004).

References

[1] Li, C.; Qi, X. S.; Gong, X.; Peng, Q.; Chen, Y. L.; Xie, R.; Zhong, W. Magnetic–dielectric synergy and interfacial engineering to design yolk–shell structured CoNi@void@C and CoNi@void@C@MoS_2 nanocomposites with tunable and strong wideband microwave absorption. *Nano Res.* **2022**, *15*, 6761–6771.

[2] Ma, Z. L.; Xiang, X. L.; Shao, L.; Zhang, Y. L.; Gu, J. W. Multifunctional wearable silver nanowire decorated leather nanocomposites for Joule heating, electromagnetic interference shielding and piezoresistive sensing. *Angew Chem., Int. Ed.* **2022**, *61*, e202200705.

[3] Lv, H. L.; Yang, Z. H.; Liu B.; Wu, G. L.; Lou, Z. C.; Fei, B.; Wu, R. B. A flexible electromagnetic wave-electricity harvester. *Nat. Commun.* **2021**, *12*, 834.

[4] Qiu, Y.; Yang, H. B.; Hu, F. F.; Lin, Y. Two-dimensional CoNi@mesoporous carbon composite with heterogeneous structure toward broadband microwave absorber. *Nano Res.* **2022**, *15*, 7769–7777.

[5] Lou, Z. C.; Wang, Q. Y.; Kara, U. I.; Mamtani, R. S.; Zhou, X. D.; Bian, H. Y.; Yang, Z. H.; Li, Y. J.; Lv, H. L.; Adera, S. et al. Biomass-derived carbon heterostructures enable environmentally adaptive wideband electromagnetic wave absorbers. *Nano-Micro Lett.* **2022**, *14*, 11.

[6] Song, P.; Ma, Z. L.; Qiu, H.; Ru, Y. F.; Gu, J. W. High-efficiency electromagnetic interference shielding of rGO@FeNi/epoxy composites with regular honeycomb structures. *Nano-Micro Lett.* **2022**, *14*, 51.

[7] Qiu, Y.; Yang, H. B.; Cheng, Y.; Lin, Y. MOFs derived flower-like nickel and carbon composites with controllable structure toward efficient microwave absorption. *Compos. Part A: Appl. Sci. Manuf.* **2022**, *154*, 106772.

[8] Hou, T. Q.; Jia, Z. R.; Dong, Y. H.; Liu, X. H.; Wu, G. L. Layered 3D structure derived from MXene/magnetic carbon nanotubes for ultra-broadband electromagnetic wave absorption. *Chem. Eng. J.* **2022**, *431*, 133919.

[9] Zhao, B.; Li, Y.; Zeng, Q. W.; Wang, L.; Ding, J. J.; Zhang, R.; Che, R. C. Galvanic replacement reaction involving core–shell magnetic chains and orientation-tunable microwave absorption properties. *Small* **2020**, *16*, 2003502.

[10] Sui, M. X.; Sun, X. D.; Lou, H. F.; Li, X. P.; Lv, X. L.; Li, L.; Gu, G. X. Synthesis of hollow Fe_3O_4 particles via one-step solvothermal approach for microwave absorption materials: Effect of reactant

concentration, reaction temperature and reaction time. *J. Mater. Sci. Mater. Electron.* **2018**, *29*, 7539–7550.

[11] Shen, J. Y.; Zhang, D. F.; Wu, Q. B.; Wang, Y.; Gao, H.; Yu, J. L.; Zeng, G. X.; Zhang, H. Y. Pyrolysis-controlled FeCoNi@hard carbon composites with facilitated impedance matching for strong electromagnetic wave response. *J. Mater. Chem. C* **2021**, *9*, 13447–13459.

[12] Sun, H.; Che, R. C.; You, X.; Jiang, Y. S.; Yang, Z. B.; Deng, J.; Qiu, L. B.; Peng, H. S. Cross-stacking aligned carbon-nanotube films to tune microwave absorption frequencies and increase absorption intensities. *Adv. Mater.* **2014**, *26*, 8120–8125.

[13] Zhao, H.; Yun, J.; Zhang, Y. L.; Ruan, K. P.; Huang, Y. S.; Zheng, Y. P.; Chen, L. X.; Gu, J. W. Pressure-induced self-interlocked structures for expanded graphite composite papers achieving prominent EMI shielding effectiveness and outstanding thermal conductivities. *ACS Appl. Mater. Interfaces* **2022**, *14*, 3233–3243.

[14] Wang, H. G.; Meng, F. B.; Huang, F.; Jing, C. F.; Li, Y.; Wei, W.; Zhou, Z. W. Interface modulating CNTs@PANi hybrids by controlled unzipping of the walls of CNTs to achieve tunable high-performance microwave absorption. *ACS Appl. Mater. Interfaces* **2019**, *11*, 12142–12153.

[15] Chen, C.; Xi, J. B.; Zhou, E. Z.; Peng, L.; Chen, Z. C.; Gao, C. Porous graphene microflowers for high-performance microwave absorption. *Nano-Micro Lett.* **2018**, *10*, 26.

[16] Wang, H. Q. Nanostructure@metal-organic frameworks (MOFs) for catalytic carbon dioxide (CO_2) conversion in photocatalysis, electrocatalysis, and thermal catalysis. *Nano Res.* **2022**, *15*, 2834–2854.

[17] Yao, M. S.; Xiu, J. W.; Huang, Q. Q.; Li, W. H.; Wu, W. W.; Wu, A. Q.; Cao, L. A.; Deng, W. H.; Wang, G. E.; Xu, G. Van der Waals heterostructured MOF-on-MOF thin films: Cascading functionality to realize advanced chemiresistive sensing. *Angew. Chem.* **2019**, *131*, 15057–15061.

[18] Lv, H. L.; Yang, Z. H.; Pan, H. G.; Wu, R. B. Electromagnetic absorption materials: Current progress and new frontiers. *Prog. Mater. Sci.* **2022**, *127*, 100946.

[19] Lei, Z. W.; Shen, J. L.; Zhang, W. D.; Wang, Q. R.; Wang, J.; Deng, Y. H.; Wang, C. Y. Exploring porous zeolitic imidazolate frame work-8 (ZIF-8) as an efficient filler for high-performance poly (ethyleneoxide)-based solid polymer electrolytes. *Nano Res.* **2020**, *13*, 2259–2267.

[20] Zhang, W.; Jiang, X. F.; Wang, X. B.; Kaneti, Y. V.; Chen, Y. X.; Liu, J.; Jiang, J. S.; Yamauchi, Y.; Hu, M. Spontaneous weaving of graphitic carbon networks synthesized by pyrolysis of ZIF-67 crystals. *Angew Chem., Int. Ed.* **2017**, *56*, 8435–8440.

[21] Li, X. H.; Wang, L.; You, W. B.; Li, X.; Yang, L. T.; Zhang, J.; Wang, M.; Che, R. C. Enhanced microwave absorption performance from abundant polarization sites of ZnO nanocrystals embedded in CNTs via confined space synthesis. *Nanoscale* **2019**, *11*, 22539–22549.

[22] Chen, H.; Hong, R.; Liu, Q. C.; Li, S. K.; Huang, F. Z.; Lu, Y.; Wang, L.; Li, K. Z.; Zhang, H. CNFs@carbonaceous Co/CoO composite derived from CNFs penetrated through ZIF-67 for high-efficient electromagnetic wave absorption material. *J. Alloys Compd.* **2018**, *752*, 115–122.

[23] Feng, W.; Wang, Y. M.; Zou, Y. C.; Chen, J. C.; Jia, D. C.; Zhou, Y. ZnO@N-doped porous carbon/Co_3ZnC core–shell heterostructures with enhanced electromagnetic wave attenuation ability. *Chem. Eng. J.* **2018**, *342*, 364–371.

[24] Lee, Y. R.; Jang, M. S.; Cho, H. Y.; Kwon, H. J.; Kim, S.; Ahn, W. S. ZIF-8: A comparison of synthesis methods. *Chem. Eng. J.* **2015**, *271*, 276–280.

[25] Zhang, Y. L.; Kong, J.; Gu, J. W. New generation electromagnetic materials: Harvesting instead of dissipation solo. *Sci. Bull.* **2022**, *67*, 1413–1415.

[26] Banerjee, R.; Phan, A.; Wang, B.; Knobler, C.; Furukawa, H.; O'Keeffe, M.; Yaghi, O. M. High-throughput synthesis of zeolitic imidazolate frameworks and application to CO_2 capture. *Science* **2008**, *319*, 939–943.

[27] Li, X. Y.; Gao, X. Y.; Ai, L. H.; Jiang, J. Mechanistic insight into the interaction and adsorption of Cr(VI) with zeolitic imidazolate framework-67 microcrystals from aqueous solution. *Chem. Eng. J.* **2015**, *274*, 238–246.

[28] Guo, J.; Gadipelli, S.; Yang, Y. C.; Li, Z. N.; Lu, Y.; Brett, D. J. L.; Guo, Z. X. An efficient carbon-based ORR catalyst from low-temperature etching of ZIF-67 with ultra-small cobalt nanoparticles and high yield. *J. Mater. Chem. A* **2019**, *7*, 3544–3551.

[29] Cui, B. Y.; Wu, G. M.; Qiu, S. J.; Zou, Y. J.; Yan, E. H.; Xu, F.; Sun, L. X.; Chu, H. L. Ruthenium supported on cobalt-embedded porous carbon with hollow structure as efficient catalysts toward ammonia-borane hydrolysis for hydrogen production. *Adv. Sustainable Syst.* **2021**, *5*, 2100209.

[30] Zhang, Z. Y.; Tan, Y. Y.; Zeng, T.; Yu, L. Y.; Chen, R. Z.; Cheng, N. C.; Mu, S. C.; Sun, X. L. Tuning the dual-active sites of ZIF-67 derived porous nanomaterials for boosting oxygen catalysis and rechargeable Zn-air batteries. *Nano Res.* **2021**, *14*, 2353–2362.

[31] Zhang, Y. T.; Wang, P.; Yang, J.; Lu, S. S.; Li, K. K.; Liu, G. Y.; Duan, Y. F.; Qiu, J. S. Decorating ZIF-67-derived cobalt-nitrogen doped carbon nanocapsules on 3D carbon frameworks for efficient oxygen reduction and oxygen evolution. *Carbon* **2021**, *177*, 344–356.

[32] Yang, S. J.; Kim, T.; Im, J. H.; Kim, Y. S.; Lee, K.; Jung, H.; Park, C. R. MOF-derived hierarchically porous carbon with exceptional porosity and hydrogen storage capacity. *Chem. Mater.* **2012**, *24*, 464–470.

[33] Qiao, B. T.; Wang, A. Q.; Yang, X. F.; Allard, L. F.; Jiang, Z.; Cui, Y. T.; Liu, J. Y.; Li, J.; Zhang, T. Single-atom catalysis of CO oxidation using Pt_1/FeO_x. *Nat. Chem.* **2011**, *3*, 634–641.

[34] Yang, Q. H.; Yang, C. C.; Lin, C. H.; Jiang, H. L. Metal-organic-framework-derived hollow N-doped porous carbon with ultrahigh concentrations of single Zn atoms for efficient carbon dioxide conversion. *Angew. Chem.* **2019**, *131*, 3549–3553.

[35] Jin, H. H.; Zhou, H.; Ji, P. X.; Zhang, C. T.; Luo, J. H.; Zeng, W. H.; Hu, C. X.; He, D. P.; Mu, S. C. ZIF-8/$LiFePO_4$ derived Fe-N-P Co-doped carbon nanotube encapsulated Fe_2P nanoparticles for efficient oxygen reduction and Zn-air batteries. *Nano Res.* **2020**, *13*, 818–823.

[36] Li, X. M.; Qiao, Y. Q.; Wang, C. H.; Shen, T. D.; Zhang, X. Y.; Wang, H. C.; Li, Y. S.; Gao, W. M. MOF-derived Co/C nanocomposites encapsulated by $Ni(OH)_2$ ultrathin nanosheets shell for high performance supercapacitors. *J. Alloys Compd.* **2019**, *770*, 803–812.

[37] Lv, H. L.; Yang, Z. H.; Ong, S. J. H.; Wei, C.; Liao, H. B.; Xi, S. B.; Du, Y. H.; Ji, G. B.; Xu, Z. J. A flexible microwave shield with tunable frequency-transmission and electromagnetic compatibility. *Adv. Funct. Mater.* **2019**, *29*, 1900163.

[38] Liu, Y.; Jia, Z. R.; Zhan, Q. Q.; Dong, Y. H.; Xu, Q. M.; Wu, G. L. Magnetic manganese-based composites with multiple loss mechanisms towards broadband absorption. *Nano Res.* **2022**, *15*, 5590–5600.

[39] Song, P.; Liu, B.; Liang, C. B.; Ruan, K. P.; Qiu, H.; Ma, Z. L.; Guo, Y. Q.; Gu, J. W. Lightweight, flexible cellulose-derived carbon aerogel@reduced graphene oxide/PDMS composites with outstanding EMI shielding performances and excellent thermal conductivities. *Nano-Micro Lett.* **2021**, *13*, 91.

[40] Sun, X. P.; Sun, S. X.; Gu, S. Q.; Liang, Z. F.; Zhang, J. X.; Yang, Y. Q.; Deng, Z.; Wei, P.; Peng, J.; Xu, Y. et al. High-performance single atom bifunctional oxygen catalysts derived from ZIF-67 superstructures. *Nano Energy* **2019**, *61*, 245–250.

[41] Ning, M. Q.; Man, Q. K.; Tan, G. G.; Lei, Z. K.; Li, J. B.; Li, R. W. Ultrathin MoS_2 nanosheets encapsulated in hollow carbon spheres: A case of a dielectric absorber with optimized impedance for efficient microwave absorption. *ACS Appl. Mater. Interfaces* **2020**, *12*, 20785–20796.

[42] Wang, X. X.; Cullen, D. A.; Pan, Y. T.; Hwang, S.; Wang, M. Y.; Feng, Z. X.; Wang, J. Y.; Engelhard, M. H.; Zhang, H. G.; He, Y. H. et al. Nitrogen-coordinated single cobalt atom catalysts for oxygen reduction in proton exchange membrane fuel cells. *Adv. Mater.* **2018**, *30*, 1706758.

[43] Peng, K. S.; Liu, C. Y.; Wu, Y. H.; Fang, G.; Xu, G. Y.; Zhang, Y. J.; Wu, C.; Yan, M. Understanding the efficient microwave

absorption for FeCo@ZnO flakes at elevated temperatures a combined experimental and theoretical approach. *J. Mater. Sci. Technol.* **2022**, *125*, 212–221.

[44] Zhao, B.; Guo, X. Q.; Zhao, W. Y.; Deng, J. S.; Fan, B. B.; Shao, G.; Bai, Z. Y.; Zhang, R. Facile synthesis of yolk–shell Ni@void@SnO_2(Ni_3Sn_2) ternary composites via galvanic replacement/Kirkendall effect and their enhanced microwave absorption properties. *Nano Res.* **2017**, *10*, 331–343.

[45] Han, Y. X.; Ruan, K. P.; Gu, J. W. Janus (BNNS/ANF)-(AgNWs/ANF) thermal conductivity composite films with superior electromagnetic interference shielding and Joule heating performances. *Nano Res.* **2022**, *15*, 4747–4755.

[46] Zhang, X. Y.; Jia, Z. R.; Zhang, F.; Xia, Z. H.; Zou, J. X.; Gu, Z.; Wu, G. L. MOF-derived $NiFe_2S_4$/porous carbon composites as electromagnetic wave absorber. *J. Colloid Interface Sci.* **2022**, *610*, 610–620.

[47] Lv, H. L.; Yang, Z. H.; Xu, H. B.; Wang, L. Y.; Wu, R. B. An electrical switch-driven flexible electromagnetic absorber. *Adv. Funct. Mater.* **2020**, *30*, 1907251.

[48] Zhang, Y. L.; Ruan, K. P.; Shi, X. T.; Qiu, H.; Pan, Y.; Yan, Y.; Gu, J. W. $Ti_3C_2T_x$/rGO porous composite films with superior electromagnetic interference shielding performances. *Carbon* **2021**, *175*, 271–280.

[49] Ning, M. Q.; Lei, Z. K.; Tan, G. G.; Man, Q. K.; Li, J. B.; Li, R. W. Dumbbell-like Fe_3O_4@N-doped carbon@2H/1T-MoS_2 with tailored magnetic and dielectric loss for efficient microwave absorbing. *ACS Appl. Mater. Interfaces* **2021**, *13*, 47061–47071.

[50] Liu, Y.; Liu, X. H.; E, X. Y.; Wang, B. B.; Jia, Z. R.; Chi, Q. G.; Wu, G. L. Synthesis of Mn_xO_y@C hybrid composites for optimal electromagnetic wave absorption capacity and wideband absorption. *J. Mater. Sci. Technol.* **2022**, *103*, 157–164.

[51] Zhao, B.; Shao, G.; Fan, B. B.; Zhao, W. Y.; Xie, Y. J.; Zhang, R. Synthesis of flower-like CuS hollow microspheres based on nanoflakes self-assembly and their microwave absorption properties. *J. Mater. Chem. A* **2015**, *3*, 10345–10352.

[52] Lv, H. L.; Yang, Z. H.; Wang, P. L.; Ji, G. B.; Song, J. Z.; Zheng, L. R.; Zeng, H. B.; Xu, Z. J. A voltage-boosting strategy enabling a low-frequency, flexible electromagnetic wave absorption device. *Adv. Mater.* **2018**, *30*, 1706343.

[53] Liu, Q. H.; Cao, Q.; Bi, H.; Liang, C. Y.; Yuan, K. P.; She, W.; Yang, Y. J.; Che, R. C. CoNi@SiO_2@TiO_2 and CoNi@Air@TiO_2 microspheres with strong wideband microwave absorption. *Adv. Mater.* **2016**, *28*, 486–490.

[54] Zhang, J. J.; Qi, X. S.; Gong, X.; Peng, Q.; Chen, Y. L.; Xie, R.; Zhong, W. Microstructure optimization of core@shell structured MSe_2/$FeSe_2$@$MoSe_2$ (M = Co, Ni) flower-like multicomponent nanocomposites towards high-efficiency microwave absorption. *J. Mater. Sci. Technol.* **2022**, *128*, 59–70.

[55] Fang, G.; Liu, C. Y.; Yang, Y.; Peng, K. S.; Cao, Y. F.; Jiang, T.; Zhang, Y. T.; Zhang, Y. J. Regulating percolation threshold via dual conductive phases for high-efficiency microwave absorption performance in C and X bands. *ACS Appl. Mater. Interfaces* **2021**, *13*, 37517–37526.

[56] Guo, Y. Q.; Qiu, H.; Ruan, K. P.; Zhang, Y. L.; Gu, J. W. Hierarchically multifunctional polyimide composite films with strongly enhanced thermal conductivity. *Nano-Micro Lett.* **2022**, *14*, 26.

[57] Li, C.; Li, Z. H.; Qi, X. S.; Gong, X.; Chen, Y. L.; Peng, Q.; Deng, C. Y.; Jing, T.; Zhong, W. A generalizable strategy for constructing ultralight three-dimensional hierarchical network heterostructure as high-efficient microwave absorber. *J. Colloid Interface Sci.* **2022**, *605*, 13–22.

[58] Sun, C. H.; Jia, Z. R.; Xu, S.; Hu, D. Q.; Zhang, C. H.; Wu, G. L. Synergistic regulation of dielectric–magnetic dual-loss and triple heterointerface polarization via magnetic MXene for high-performance electromagnetic wave absorption. *J. Mater. Sci. Technol.* **2022**, *113*, 128–137.

[59] Wen, C. Y.; Li, X.; Zhang, R. X.; Xu, C. Y.; You, W. B.; Liu, Z. W.; Zhao, B.; Che, R. C. High-density anisotropy magnetism enhanced microwave absorption performance in $Ti_3C_2T_x$ MXene@Ni microspheres. *ACS Nano* **2022**, *16*, 1150–1159.

[60] Zhou, X. D.; Han, H.; Wang, Y. C.; Zhang, C.; Lv, H. L.; Lou, Z. C. Silicon-coated fibrous network of carbon nanotube/iron towards stable and wideband electromagnetic wave absorption. *J. Mater. Sci. Technol.* **2022**, *121*, 199–206.

[61] Zhou, Y.; Deng, X.; Xing, H. N.; Zhao, H. Y.; Liu, Y. B.; Guo, L. S.; Feng, J.; Feng, W.; Zong, Y.; Zhu, X. H. et al. Dynamically observing the formation of MOFs-driven Co/N-doped carbon nanocomposites by *in-situ* transmission electron microscope and their application as high-efficient microwave absorbent. *Nano Res.* **2022**, *15*, 6819–6830.